Birefringence Analysis of Photonic-Bandgap Fibers Using the Hexagonal Yee's Cell

Kiarash Zamani Aghaie, *Student Member, IEEE*, Shanhui Fan, *Senior Member, IEEE*, and Michel J. F. Digonnet

***Abstract*—A full-vectorial finite-difference scheme utilizing the hexagonal Yee's cell is used in this paper to analyze the modes of photonic-bandgap fibers with C_{6v} symmetry. Because it respects the fiber's native symmetry, this method is free from any numerical birefringence. We also incorporate in it techniques for reducing the memory requirement (up to 3 to 4 times) and computational time, in particular by exploiting some of the symmetry properties of these fibers. Using sub-pixel averaging, we demonstrate quadratic convergence for the fundamental mode's effective index dependence on spatial resolution. We show that this method can be used to calculate the beat length of PBFs in which a birefringence is introduced by applying a small unidirectional stretch to the fiber cross section along one of its axes. Abrupt variations of the modeled fiber geometries with spatial resolution lead to oscillatory beat length convergence behavior. We can obtain a better estimate for beat length by averaging these oscillations. We apply a strong perturbation analysis to the fiber's unperturbed mode, calculated by our finite-difference method, to perform this averaging in a rigorous way. By fitting a polynomial to the predicted beat lengths as a function of grid spacing, we obtain an accurate estimate of the beat length at zero grid spacing. Reasonable convergence for the beat length is observed using a single processor with 8 GB of memory.**

***Index Terms*—Birefringence, elliptical waveguides, finite difference methods, optical fibers, waveguide theory.**

I. Introduction

SINCE photonic-bandgap fibers (PBFs) were first experimentally demonstrated in 1996 [1], they have attracted a great deal of interest both in theoretical and experimental work. A distinctive structural feature of many photonic-bandgap fibers, including some of the most widely used geometries, is their C_{6v} symmetry, i.e., six-fold rotational and reflection symmetry (at least in the idealized case). This symmetry results in an exact double degeneracy of the fundamental modes [2], [3]. Small perturbations that break this C_{6v} symmetry, for example a slight ellipticity of the core region, lift this degeneracy and introduce birefringence. This kind of perturbation may be the origin of the fairly large birefringence reported in a variety of air-core fibers, for example the difference of 10^{-5} between effective indexes of the two fundamental modes reported in [4]. Since birefringence has a significant impact on many applications involving fiber, being able to predict this birefringence for a given perturbation is of great importance for the design of photonic-bandgap fibers.

In general, since the birefringence is small compared with the effective index of the modes, it is significantly more challenging to determine the birefringence accurately than the modal effective index. As a starting point, one should use a numerical method that has no numerical birefringence, namely, for a fiber without physical birefringence, the method should predict that the doubly-degenerate fundamental modes have essentially the same effective index. Several numerical methods have been utilized to study the modal dispersion of solid-core photonic-crystal fibers (PCFs) and photonic-bandgap fibers. These include the plane-wave expansion (PWE) [5]–[7], the finite-element method (FEM) [4], [8]–[10], the beam-propagation method (BPM) [11], the finite-difference time-domain method (FDTD) [12], the multipole method [13]–[15], and the finite-difference frequency-domain method (FDFD) [16]–[18]. Although the majority of these methods have been demonstrated for PCFs only, they are applicable for realistic PBFs as well. The only exception is the multipole method, which is limited to PBFs with circular holes that are relatively small and hence the structures have thick core rings [19]. Most of these methods involve discretizing space on a numerical grid and describing the permittivity profile of the fiber transverse cross section on this grid [4]–[18]. This grid can be square [5], [12], [16]–[18], or hexagonal [7], or it can consist of curvilinear hybrid edge/nodal elements [10], [11] or triangular elements [4], [8], [9]. In order to most accurately describe the modal properties of a photonic-bandgap fiber, the grid should have the same symmetry as the fiber. It has been shown [4], [6], [10], [16], [20] that for a fiber with C_{6v} symmetry, failing to use a grid with this symmetry leads to substantial numerical birefringence.

Only a few of these methods predict zero numerical birefringence for a photonic-bandgap fiber with C_{6v} symmetry [4], [7], including the multipole method [19]. In the PWE method proposed in [7], the permittivity profile of the fiber was discretized using a hexagonal non-uniform grid that preserves the fiber symmetry. In [4], a holey optical fiber was studied with a finite-element method that respects the hexagonal symmetry of the fiber. However, there have been very few investigations of the birefringence of photonic-bandgap fibers [21], [22]. Both of these studies are based on the finite-element method. The refractive index profile of the fiber was discretized on a non-uniform grid that has its highest density on the dielectric interfaces. This method is particularly well suited for fiber structures with sharp

Manuscript received October 08, 2009; revised December 18, 2009. Current version published March 10, 2010. This work was supported by Litton Systems, Inc., a wholly owned subsidiary of Northrop Grumman Corporation.

The authors are with the Edward L. Ginzton Laboratory, Stanford University, Stanford, CA 94305 USA (e-mail: kzamani@stanford.edu; shanhui@stanford.edu; silurian@stanford.edu).

Color versions of one or more of the figures in this paper are available online at http://ieeexplore.ieee.org.

Digital Object Identifier 10.1109/JQE.2010.2040369

corners or very thin membranes. However, neither the convergence of the birefringence predicted with these methods nor the computational time has been reported.

FDFD is another well-known method for modeling photonic-bandgap fibers [16]–[18]. The advantages of FDFD are that implementation and parallelization is straightforward, and that it has a high modeling efficiency [16], [18]. Since a rectangular grid has been conventionally used in FDFD methods for modeling PBFs, all of the previously published FDFD methods suffer from a very high numerical birefringence. The main purpose of this paper is to implement this method with a hexagonal grid and show, for the first time, that it can accurately model the birefringence of photonic-bandgap fibers. Our aim is not to establish that this method is superior to previously published methods. Other, and perhaps all, methods have their place in the numerical analysis of these fibers and constitute a useful tool to model certain geometries with a specific set of features. The main objective of this manuscript is first to describe in some detail the principle of this method, and second to document, through numerical studies of photonic-bandgap fibers, the basic features of this method, including convergence, accuracy, coding requirements, and computation time on specific computer systems. This archival work can later be used as a reference to compare these features with those of other methods.

In order to model the birefringence of photonic-bandgap fibers with slightly elliptical cross section using FDFD, we apply four major modifications to this method. First, we utilize a hexagonal Yee's grid to model the effective indexes of the modes of unperturbed photonic-bandgap fibers with perfect C_{6v} symmetry. Second, we introduce sub-pixel averaging [23] to improve the convergence behavior. We show that with this choice of grid, the numerical birefringence normally present when using other grid geometries (e.g., square) is completely removed, as expected from [20]. Moreover, this method involves finding the eigenvalues of large sparse matrices. With the use of available software packages such as ARPACK, modeling of realistic fiber geometries can be done on a single-processor computer with a relatively high speed. To the best of our knowledge, it is the first report that the hexagonal Yee's grid removes the numerical birefringence in the FDFD analysis of the fundamental mode of photonic-bandgap fibers.

The method we used for modeling birefringence is to apply a unidirectional stretch to the fiber cross section and model this perturbed fiber with our FDFD method. The beat length predicted by this approach has an oscillatory convergence behavior. This is possibly due to the large variations in the discretized permittivity profile of a fiber with slight ellipticity as the spatial resolution changes. However, we show that this method provides reasonable beat length prediction at high enough spatial resolutions. To obtain a smooth beat length convergence behavior, we introduced a third major modification to our FDTD method, which consisted in applying a strong perturbation method [24] to the modes of the unperturbed fiber predicted by the FDFD method. We establish that this new method predicts the modal birefringence with a reasonable accuracy for small ellipticities. As the fourth improvement, we fit the predicted beat lengths at different grid spacings to a polynomial to obtain an estimate of the beat length at zero grid spacing, and, hence, the error in our predicted results.

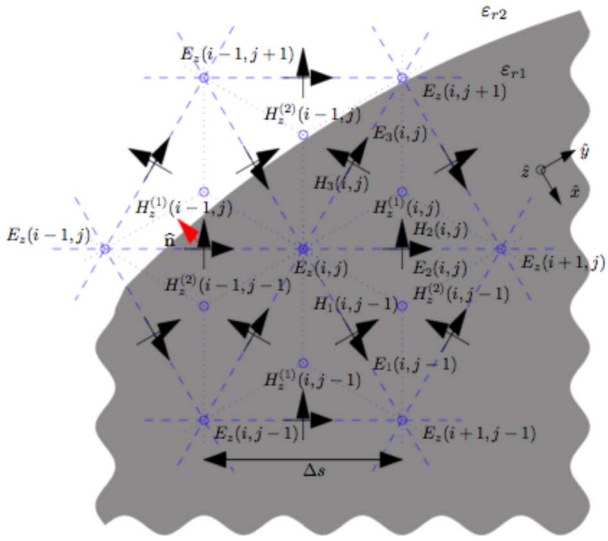

Fig. 1. The hexagonal Yee's grid along with a dielectric interface between two regions with permittivities ε_{r1} (gray) and ε_{r2} (white). Dual cells are shown with dotted lines. $\hat{\mathbf{n}}$ (red arrow) is the unit-normal vector perpendicular to the interface at the grid point where $E_2(i-1,j)$ and $H_2(i-1,j)$ are defined.

II. The Finite-Difference Formulation Using the Hexagonal Yee's Cell With No Averaging

Fig. 1 shows the hexagonal Yee's grid used in this paper. The z axis is the longitudinal direction of the fiber. In the same manner as when using a square Yee's grid, the different field components are labeled with two indexes i and j. The first index i sweeps the fields along the horizontal direction, while the second index j sweeps the fields at 60° to the horizontal axis. The longitudinal electric fields, e.g., $E_z(i,j)$ in Fig. 1, are defined on a triangular lattice of grid points with a lattice constant Δs. The transverse electric and magnetic field components are defined at the edges of the triangles, e.g., $E_2(i,j)$ and $H_2(i,j)$.

Since this grid has three non-equivalent sites on its edges (i.e., sites that are not related by the grid's translational symmetry), there are three transverse electric and three transverse magnetic fields per unit cell, namely transverse electric fields $E_1(i,j-1)$, $E_2(i,j)$, and $E_3(i,j)$ and transverse magnetic fields $H_1(i,j-1)$, $H_2(i,j)$, and $H_3(i,j)$ (see Fig. 1). The longitudinal magnetic fields are defined at the centers of the triangles. Since there are two non-equivalent center sites in each unit cell of the triangular lattice, there are also two longitudinal magnetic components, e.g., $H_z^{(1)}(i,j)$ and $H_z^{(2)}(i-1,j)$ (see Fig. 1). This is in contrast with a conventional square Yee's grid, in which there are only two transverse electric and magnetic fields and one longitudinal E_z and H_z fields per unit cell.

In the FDFD method utilizing Yee's grid, one needs to formulate a discretized version of Maxwell's equations into an eigenvalue equation in terms of either transverse magnetic or transverse electric fields. Since there are three independent transverse fields in a hexagonal Yee's grid, the final eigenvalue equation will be expressed in terms of three transverse fields, i.e., the fields E_1, E_2, and E_3 or H_1, H_2, and H_3 shown in Fig. 1.

TABLE I
PERMUTATION TABLE FOR THE DISCRETIZED FIELD COMPONENTS

Original value	$E_2(i,j)$	$H_2(i,j)$	$E_1(i,j-1)$	$H_1(i,j-1)$	$E_3(i,j)$	$H_3(i,j)$	$H_z^{(2)}(i,j-1)$	$H_z^{(1)}(i,j)$
Permuted value	$E_3(i,j)$	$H_3(i,j)$	$E_2(i,j)$	$H_2(i,j)$	$-E_1(i-1,j)$	$-H_1(i-1,j)$	$H_z^{(1)}(i,j)$	$H_z^{(2)}(i-1,j)$

The translational symmetry of the fiber along the z direction requires the fields to have an $e^{j(\omega t-\beta z)}$ dependence, where ω is the optical frequency and β is the propagation constant along z. Two independent Maxwell's curl equations, $\nabla\times\mathbf{H}=j\omega\epsilon_o\varepsilon_r\mathbf{E}$ and $\nabla\times\mathbf{E}=-j\omega\mu_o\mathbf{H}$, are sufficient for the characterization of the propagating modes of an optical fiber. We assume that the optical fiber is made from an *isotropic* dielectric. Either the differential form or the integral form of these equations can be used for finding discretized FDFD equations. We used the integral form because it is easier to implement with a hexagonal grid.

We first evaluate the equation $\int_S j\omega\epsilon_o\varepsilon_r\mathbf{E}\cdot d\mathbf{S}=\oint\mathbf{H}\cdot d\mathbf{l}$, at the locations where $E_z(i,j)$ and $E_2(i,j)$ are defined, using a surface region S that is normal to the electric field and centered at the electric field location. This leads to (1)–(2), shown at the bottom of the page, in which $\varepsilon_{rz}(i,j)$ and $\varepsilon_{r2}(i,j)$ are the permittivity of the structure at the point where E_z and E_2 are defined, respectively. Note that in (2) the propagation constant β appears when the integration surface is normal to the transverse plane due to differentiation along the longitudinal direction. Two equations similar to (2) can be obtained by direct evaluation of this integral equation at the locations where $E_1(i,j)$ and $E_3(i,j)$ are defined. Instead, for simplicity, we chose to use the symmetry of hexagonal Yee's grid to arrive at these same equations. Table I shows the permutation of all discretized fields required for obtaining these equations. The fields in the second row are the ones in the first row rotated counter-clockwise by 60° about the point where $E_z(i,j)$ is defined. Using this table, one can obtain the equation equivalent to (2) written for $E_3(i,j)$ by substituting the fields in (2) by their corresponding values shown in the second row of the table. In addition, substitution of the fields in (2) with their corresponding values shown in the first row yields the relation written for $E_1(i,j)$. For conciseness, we henceforth discuss the discretized equations just for two transverse fields, i.e., E_2 and H_2, and one longitudinal magnetic field, i.e., $H_z^{(1)}$. The relations for other field components can be easily obtained using Table I as just described.

Similarly, for $-\int_S j\omega\mu_o\mathbf{H}\cdot d\mathbf{S}=\oint\mathbf{E}\cdot d\mathbf{l}$ one obtains:

$$-j\omega\mu_o H_2(i,j)=-j\beta E_2(i,j)-\frac{E_z(i+1,j)-E_z(i,j)}{\Delta s} \tag{3}$$

$$-j\omega\mu_o H_z^{(1)}(i,j)=4\frac{E_2(i,j)-E_1(i,j)-E_3(i,j)}{\sqrt{3}\Delta s}. \tag{4}$$

Eliminating E_z from (3) using (1), we obtain the following relation:

$$\begin{aligned}\beta E_2(i,j)=\omega\mu_\circ\Big\{&H_2(i,j)\\&+\frac{2}{3k_\circ^2\Delta s^2\varepsilon_{rz}(i+1,j)}\Big[H_1(i+1,j-1)\\&-H_1(i,j)+H_2(i+1,j)\\&-H_2(i,j)+H_3(i+1,j)\\&-H_3(i+1,j-1)\Big]\\&-\frac{2}{3k_o^2\Delta s^2\varepsilon_{rz}(i,j)}\Big[H_1(i,j-1)\\&-H_1(i-1,j)+H_2(i,j)\\&-H_2(i-1,j)+H_3(i,j)\\&-H_3(i,j-1)\Big]\Big\}\end{aligned} \tag{5}$$

where $k_o=\omega/c$. Similarly, the elimination of $H_z^{(1)}$ and $H_z^{(2)}$ from (2) using (4) and the corresponding equation for $H_z^{(2)}$ leads to

$$\begin{aligned}\beta H_2(i,j)=\frac{1}{\omega\mu_o}\Bigg[&\frac{4}{\Delta s^2}(E_1(i,j)+E_1(i,j-1))\\&+\left(k_o^2\varepsilon_{r2}(i,j)-\frac{8}{\Delta s^2}\right)E_2(i,j)\\&+\frac{4}{\Delta s^2}(E_3(i+1,j-1))\Bigg].\end{aligned} \tag{6}$$

As detailed in Section III, (5) and (6) and the equivalent expressions for the other field components, for all grid points in a particular computational window, can be written in a matrix form. The eigenvalues and eigenvectors of this matrix yield the modes' effective indexes and their field profiles.

III. FINITE-DIFFERENCE FORMULATION WITH SUB-PIXEL AVERAGING

For most structures, the interfaces between two isotropic dielectrics do not coincide with a grid plane. Accurate description

$$j\omega\epsilon_o\varepsilon_{rz}(i,j)E_z(i,j)=2\frac{H_1(i,j-1)-H_1(i-1,j)+H_2(i,j)-H_2(i-1,j)+H_3(i,j)-H_3(i,j-1)}{3\Delta s} \tag{1}$$

$$j\omega\epsilon_o\varepsilon_{r2}(i,j)E_2(i,j)=j\beta H_2(i,j)+\sqrt{3}\frac{H_z^{(1)}(i,j)-H_z^{(2)}(i,j-1)}{\Delta s} \tag{2}$$

of such structures therefore requires assigning an index of refraction to grid points located near such interfaces, using for example an index-averaging scheme. In [23], Farjadpour *et al.* proposed to calculate the effective refractive index of such a point by using sub-pixel averaging, which they applied to a finite-difference scheme with the square Yee's cell. They showed that sub-pixel averaging improves the convergence rate more effectively than other averaging schemes [23]. In this section, we reformulate the finite-difference formulation discussed in the last section to implement sub-pixel averaging to the hexagonal Yee's cell.

Sub-pixel averaging is an anisotropic smoothing scheme: at a given point on the grid, it assigns a different refractive index to different field components. To do so, an averaged permittivity tensor (rather than a single value of an average index) is associated to grid points in close proximity to the interface between two isotropic dielectrics. The off-diagonal elements of this tensor are in general non-zero only for the transverse components of the discretized electric fields [23].

Consider the interface between two isotropic dielectrics with permittivities ε_{r1} and ε_{r2} shown in Fig. 1. The averaged permittivity tensor, obviously, relates the discretized components of the displacement vector to the discretized components of the electric field vector. The discretized component of the displacement vector $D_2(i,j)$ can be expressed in terms of the discretized transverse electric fields $E_2(i,j)$ according to

$$D_2(i,j) = \epsilon_o \left(\varepsilon_{r2\|}(i,j)E_2(i,j) + \varepsilon_{r2\perp}(i,j)E_{2\perp}(i,j)\right) \quad (7)$$

where $\varepsilon_{r2\|}(i,j)$ and $\varepsilon_{r2\perp}(i,j)$ are elements of the permittivity tensor, and $E_{2\perp}(i,j)$ is the electric field component in the direction perpendicular to E_2 and discretized at the point where $E_2(i,j)$ is defined. The unit-normal vector perpendicular to the interface at this point is denoted by $\hat{\mathbf{n}}$ in this figure. Let's define $n_{2\|}$ and $n_{2\perp}$ as the magnitude of the projection of this vector onto the unit vector in the direction parallel and perpendicular to E_2, respectively. According to [23], $\varepsilon_{2\|}$ and $\varepsilon_{2\perp}$ are given by

$$\varepsilon_{r2\|} = n_{2\|}^2\varepsilon_N + n_{2\perp}^2\varepsilon_P \quad (8)$$

$$\varepsilon_{r2\perp} = n_{2\|}n_{2\perp}(\varepsilon_N - \varepsilon_P) \quad (9)$$

where $\varepsilon_p = f_1\varepsilon_{r1} + f_2\varepsilon_{r2}$, $1/\varepsilon_N = f_1/\varepsilon_{r1} + f_2/\varepsilon_{r2}$, and f_1 and $f_2 = 1 - f_1$ are the permittivity filling ratios of regions 1 and 2, respectively, in the dotted dual cell centered on the point where E_2 is defined.

Note that $E_{2\perp}(i,j)$ in (7) has not been originally defined in the hexagonal Yee's grid, but it can be approximated from the neighboring discretized field components as follows:

$$E_{2\perp}(i,j) = \frac{1}{2\sqrt{3}}\Big(E_3(i,j) + E_3(i+1,j-1) - E_1(i,j) - E_1(i,j-1)\Big). \quad (10)$$

The equations for D_1 and D_3 can be obtained by changing the subscripts in (7) from 2 to 1 and 3, respectively. The expressions for $\varepsilon_{r1\|}$, $\varepsilon_{r1\perp}$, $\varepsilon_{r3\|}$ and $\varepsilon_{r3\perp}$ are also identical to (8) and (9), provided subscript 2 is substituted by 1 and 3, respectively. One just needs to compute the filling ratios in the dual cells centered at the point where E_1 and E_3 are defined, and calculate the projection of $\hat{\mathbf{n}}$ onto the unit vectors in the direction parallel and perpendicular to E_1 and E_3, respectively.

As can be seen, sub-pixel averaging requires finding the normal to the dielectric interfaces. In our applications, we calculated this normal vector analytically, which is straightforward when modeling a fiber with circular holes. For more complicated hole shapes, this normal can be evaluated by calculating numerically the integral $\oint \mathbf{r}\varepsilon(\mathbf{r})$ over the perimeter of a small circle centered at the grid point, where $\mathbf{r}$ is the vector from the center of the circle [25].

To implement sub-pixel averaging scheme, we need to modify (5), (6), and the corresponding equations for other transverse fields, so that they account for an anisotropic dielectric with such a permittivity tensor. Note that (3) and (4), which are derived from the discretization of $\nabla \times \mathbf{E} = -j\omega\mu_o\mathbf{H}$ (independent of refractive index), remain unchanged. On the other hand, the other Maxwell's curl equation is modified as $\nabla \times \mathbf{H} = j\omega\mathbf{D}$, where $\mathbf{D} = \epsilon_o\bar{\bar{\varepsilon}}\mathbf{E}$ is the displacement vector. Consequently, discretized displacement vector components should be used in (1) and (2). However, since the off-diagonal elements of the permittivity tensor used in the sub-pixel averaging are zero for the longitudinal component of the electric field, $D_z = \epsilon_o\varepsilon_{rz}E_z$, and hence, (1) still holds. Therefore, (5), which is derived from (1) and (3), remains unchanged. In contrast, (6), obtained from (2), (4), and the corresponding equation for $H_z^{(2)}$, becomes:

$$\beta H_2(i,j) = \frac{1}{\omega\mu_o}\Bigg[\frac{4}{\Delta s^2}(E_1(i,j) + E_1(i,j-1)) + \frac{k_o^2}{\epsilon_o}D_2(i,j) - \frac{8}{\Delta s^2}E_2(i,j) + \frac{4}{\Delta s^2}(E_3(i,j) + E_3(i+1,j-1))\Bigg]. \quad (11)$$

Note that two other equations similar to (11) hold for other discretized transverse field components. These relations can be obtained using Table I, and noting that the permutation rules for $D_2(i,j)$ are the same as the ones for $E_2(i,j)$ shown in Table I. Hence, these rules are obtained by substituting D_2 by E_2. Moreover, since $E_{2\perp}(i.j)$ is parallel to $H_2(i,j)$, the permutations of the former is obtained by substituting H_m by $E_{m\perp}(m = 1,2,3)$ in Table I.

Substituting (7) and (10) into (11), one obtains the following relation as the final reformulated version of (6):

$$\beta H_2(i,j) = \frac{1}{\omega\mu_o}\Bigg[\left(\frac{4}{\Delta s^2} - \frac{k_o^2\varepsilon_{r2\perp}(i,j)}{2\sqrt{3}}\right)\cdot(E_1(i,j) + E_1(i,j-1)) + \left(k_o^2\varepsilon_{r2\|}(i,j) - \frac{8}{\Delta s^2}\right)E_2(i,j) + \left(\frac{k_o^2\varepsilon_{r2\perp}(i,j)}{2\sqrt{3}} + \frac{4}{\Delta s^2}\right)\cdot(E_3(i,j) + E_3(i+1,j-1))\Bigg]. \quad (12)$$

When no averaging is used, the off-diagonal elements of the permittivity tensor are zero ($\varepsilon_{r1\perp}(i,j) = \varepsilon_{r2\perp}(i,j) = \varepsilon_{r3\perp}(i,j) = 0$), and (12) reduces to the equation derived for isotropic media (6), as expected.

Either the set of (5), (6), and their equivalents for other transverse fields (isotropic case, no averaging) or the set of (5), (12) and their equivalents (pixel-averaged expressions), can be written in a general matrix form:

$$\beta \begin{pmatrix} \mathbf{E}_1 \\ \mathbf{E}_2 \\ \mathbf{E}_3 \end{pmatrix} = \mathbf{M}_1 \begin{pmatrix} \mathbf{H}_1 \\ \mathbf{H}_2 \\ \mathbf{H}_3 \end{pmatrix} \tag{13}$$

$$\beta \begin{pmatrix} \mathbf{H}_1 \\ \mathbf{H}_2 \\ \mathbf{H}_3 \end{pmatrix} = \mathbf{M}_2 \begin{pmatrix} \mathbf{E}_1 \\ \mathbf{E}_2 \\ \mathbf{E}_3 \end{pmatrix} \tag{14}$$

in which $\mathbf{E}_1$, $\mathbf{E}_2$, $\mathbf{E}_3$ and $\mathbf{H}_1$, $\mathbf{H}_2$, $\mathbf{H}_3$ are arrays consisting of all the transverse electric and transverse magnetic fields at all grid points, respectively. Combining (13) and (14), we arrive at the eigenvalue equations whose solutions yield either transverse electric or transverse magnetic fields:

$$\beta^2 \begin{pmatrix} \mathbf{H}_1 \\ \mathbf{H}_2 \\ \mathbf{H}_3 \end{pmatrix} = \mathbf{M}_2\mathbf{M}_1 \begin{pmatrix} \mathbf{H}_1 \\ \mathbf{H}_2 \\ \mathbf{H}_3 \end{pmatrix} \tag{15}$$

$$\beta^2 \begin{pmatrix} \mathbf{E}_1 \\ \mathbf{E}_2 \\ \mathbf{E}_3 \end{pmatrix} = \mathbf{M}_1\mathbf{M}_2 \begin{pmatrix} \mathbf{E}_1 \\ \mathbf{E}_2 \\ \mathbf{E}_3 \end{pmatrix}. \tag{16}$$

The eigenvalues of these matrices give the propagation constants, and hence the effective indexes $n_{\text{eff}} = \beta/k_o$, of all the modes of the structure. The eigenvectors of these matrices give the field profile of the propagating modes.

IV. Using Symmetries to Reduce the Computational Window

We illustrate the performance of this computational scheme by applying it to calculate the modes of the photonic-bandgap fiber of Fig. 2(a). It consists of a core surrounded by a photonic-crystal cladding consisting of a periodic array of identical air holes with a period Λ. We applied the supercell method, by which the structure is replicated periodically in space (Fig. 2(b)). The computational window then consists of a single unit cell of the structure, with periodic boundary conditions applied at the edges of the window (Fig. 2(c)). The supercell method gives an accurate description of a single fiber when the size of the window is chosen to be large enough that mode coupling between adjacent cells is negligible. The choice of computational window is not unique. For example, instead of the hexagonal window of Fig. 2(c), one could choose a rhombus-shaped window (Fig. 2(d)). These two windows are equivalent because they define exactly the same periodic structure. Note that the areas of these two windows are identical.

To reduce the computational cost, it is beneficial to make use of the symmetries of the structure to reduce the size of the computational window as much as possible. For this purpose, it is important to make a distinction between the symmetry of the structure and the symmetry of its modes. For this fiber structure, which has C_{6v} symmetry, the hexagon-shaped window of Fig. 2(c) is conventionally used. The modes of an arbitrary fiber can be classified according to the irreducible representations of the symmetry group of the fiber geometry [2]. According to these representations, the modes of a fiber with C_{6v} symmetry can be classified into four classes of singly degenerate modes and two classes of doubly degenerate modes [2]. The singly degenerate modes have the full symmetry of the lattice. Consequently, only 1/12 of the computational window is needed to compute these modes. On the other hand, modes that are doubly degenerate do not have the full symmetry of the lattice, and for these modes one needs to use 1/6 of the computational window [20].

We are also interested in structures with C_{2v} symmetry, for example a twin-core PBF. To model such structures, it is natural to use the rhombus-shaped computational window (Fig. 2(d)) instead, then to invoke the mirror symmetries to limit calculations to the right-angle triangular region (black dashed region in Fig. 2(d)). Since this region occupies only 1/4 of the full window, the computational time and the required memory are reduced. Although by using 1/6 of the computational window shown in Fig. 2(c) the computational time and the required memory would be even further reduced, we chose to use 1/4 of the computational window to be able to analyze with the same code structures with either C_{6v} or C_{2v} symmetry. Using only 1/4 of the computational window reduces the memory requirement by a factor of 3 to 4.

The C_{2v} group has four irreducible representations, corresponding to the modes that satisfy either perfect electric conductor (PEC) or perfect magnetic conductor (PMC) on the two mirror planes of the structures. To describe each class of modes, we need to apply the appropriate boundary condition to each of the mirror planes. Therefore, to calculate all the modes of the fiber one would need to repeat the calculations four times, each one with different boundary conditions, on the same computational window. However, it is known that the fundamental modes satisfy the PEC boundary condition on one of the mirror planes and the PMC condition on the other. To study these modes, one only needs to do the calculation twice, once with PEC on one mirror plane and PMC on the other one, and a second time with the boundary conditions in the reverse order.

To construct the system matrix in the right-triangle-shaped computational window of Fig. 2(d), we must use *only* the fields inside the computational window. When applying the discretized equations derived above to construct this matrix, whenever the value of a field component that lies outside the computational window is needed, we must determine this value through the use of either the mirror symmetry, the periodic boundary conditions, or a combination of them. When applying the PEC boundary condition, the signs of the parallel electric field and perpendicular magnetic field are flipped, while the signs of the perpendicular electric fields and parallel magnetic fields are preserved. The opposite holds when applying the PMC boundary conditions.

Our implementation, consequently, is organized as follows: we first consider the entire rhombus-shaped region. For each grid point (i,j), we determine whether the transverse fields at this point are inside the triangular computational window. If the

field is inside, we construct a one-dimensional index of its location. We do so for all transverse fields and for all four combinations of PEC and PMC boundary conditions. In this process, one must exclude the transverse fields that are zero right at the boundaries. (Consequently, this construction depends on the boundary conditions.) This one-dimensional index is then used to construct the matrices $\mathbf{M}_1$ and $\mathbf{M}_2$. In general, a matrix element of either $\mathbf{M}_1$ or $\mathbf{M}_2$ relates two different field components. If the field is outside the triangular window, we first determine the appropriate corresponding field component that lies inside as related by the boundary conditions, then use the one-dimensional index constructed above to determine the appropriate matrix elements. The matrices $\mathbf{M}_1, \mathbf{M}_2$ thus constructed, and their products, are all sparse matrices. The eigenvalues and eigenvectors of such sparse matrix are calculated efficiently with the implicitly restarted Arnoldi method using the ARPACK Fortran library.

V. Birefringence Analysis of PBFs by Direct Application of the Proposed FDFD Method

The above-mentioned FDFD method with sub-pixel averaging was implemented in C++ and run on a variety of computers. The results in this paper were obtained using Stanford's Sun Fire X4100 Unix cluster with 8 GB of memory. With this amount of memory, we could study fibers with up to 1360 grid points along the side of computational window. On a 32-bit single processor with 4 GB of memory, fibers could be modeled with up to 800 grid points. We have also run our code on the 2.6-GHz dual-core AMD cluster of Cray XT3 MPP parallel processors at Pittsburgh supercomputing center.

To verify the accuracy of our method, we first used it to model a simpler step-index fiber, for which exact solutions for the modes' effective indexes exist. We considered a step-index fiber operating at $\lambda = 1.5$ μm, with a cylindrical silica core (refractive index 1.45) of radius $a = 3$ μm and an air cladding. Simulations were carried out with a rhombus-shaped computational window with each side equal to 12 μm. For conciseness, we have not plotted the convergence behavior of the effective index of the fundamental mode. The convergence is very smooth, and sub-pixel averaging restores the quadratic convergence rate for the effective index. For 800 grid points, which corresponds to a grid spacing $\Delta s = \lambda/100 = 15$ nm, the effective index converges to the seventh decimal.

As discussed earlier, our code can analyze structures with either C_{2v} or C_{6v} symmetries. Hence, the most straightforward approach to study birefringence in PBFs is to directly use our FDFD code with the fiber geometry with broken C_{6v} symmetry. We tried this approach for studying the birefringence of the aforementioned step-index fiber when its core is stretched 1% along an arbitrary radial axis. The convergence of the predicted beat length for this perturbed fiber is shown in Fig. 3. The birefringence of this simple fiber, predicted exactly using Mathieu elliptical functions [26], [27], is 11.22 cm (dashed line in Fig. 3). As can be seen, the beat length predicted by the direct approach generally oscillates around the theoretically predicted value. We believe that these large oscillations are due to abrupt variations of the fiber geometry caused when the grid size is varied. The magnitude of the oscillations in this figure decreases as the spatial resolution is increased. This magnitude is quite small for spatial resolutions greater than 100 points per wavelength. For example, the average error for grid spacings between $\Lambda/100$ and $\Lambda/170$ is only 2.1%. One can therefore average these oscillations to obtain a better estimate of the beat length. Doing so for spatial resolutions greater than 100 yields a beat length of 11.19 cm, or an error of only 0.3%. This shows that the FDFD method provides an accurate estimate of the beat length when applied to a conventional fiber.

Using our code, we also studied the air-core fiber shown in Fig. 2. The fiber has a hole radius of $\rho = 0.47\Lambda$, and an air core is surrounded by a smooth ring with a minimum thickness equal to 0.06Λ. The dispersion curves calculated for all the modes of this fiber are plotted in Fig. 4. The two dashed curves represent the cladding's high and low limits, and the dotted line is the light line. The dispersion curves were calculated at 20 wavelengths within the bandgap for the fundamental mode, for the combination of all four boundary conditions, and at a spatial resolution of $\Lambda/170$. At each wavelength, and for each set of boundary conditions, we calculated 15 modes, which took around 40 minutes on Stanford's Sun Fire X4100 Unix cluster with two 2.7 GHz quad-core AMD Opteron processors. The total time for computing all the dispersion curves was 53 hours on a single core. The numerical birefringence error of our method is typically less than 10^{-10} for all spatial resolutions. This fiber supports a single doubly degenerate mode from $\lambda_1 = 0.59\Lambda$ to $\lambda_2 = 0.69\Lambda$, as well as a number of surface modes that cross the fundamental-mode dispersion curve at wavelengths close to λ_2. Consequently, we studied the convergence behavior of the predicted beat length at wavelengths close to and far from surface modes. This unperturbed fiber was analyzed in a quarter of the rhombus-shaped computational window shown in Fig. 2(d) with a side length of 8Λ. Using 8 GB of memory, we could model the fiber up to a maximum spatial resolution of $\Lambda/170$. To study the birefringence of this fiber, we stretched the whole fiber geometry 1% along the y axis (see Fig. 1). The convergence of the predicted beat length of the fundamental mode at $\lambda = 0.62\Lambda$ ($\Lambda = 3.8$ μm) is plotted in Fig. 5. At this wavelength, the mode is far from the surface modes, and, hence, is only weakly or not affected by them. Here also, the convergence behavior is oscillatory. These oscillations occur for all wavelengths inside the bandgap, including where the mode is affected by the surface modes. However, the magnitude of these oscillations is again quite low for high spatial resolutions. We can again obtain a better estimate of the beat length by averaging these oscillations. Instead of averaging, we used a perturbation method, described in Section VI, which is in essence a rigorous way to perform this averaging.

VI. Strong Perturbation for the Birefringence Analysis of PBFs

The standard (weak) perturbation method fails to accurately predict birefringence when applied for the study of shifts in the dielectric interfaces between two dielectrics with a *high* index contrast [24], as is the case of a PBF made of air holes and silica.

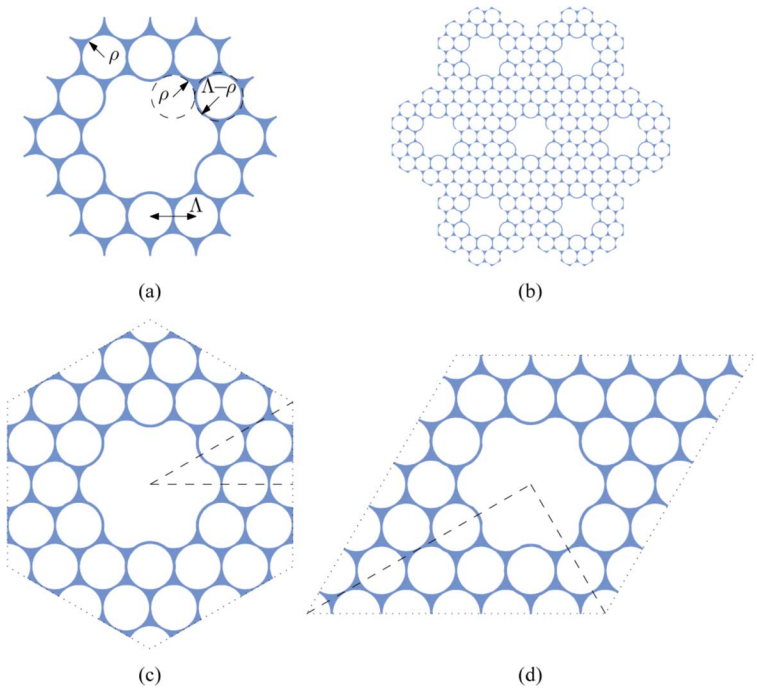

Fig. 2. (a) An air-core fiber with a scalloped ring around the core and hole radius of $\rho = 0.47\Lambda$. (b) The fiber of (a) periodically replicated on a hexagonal lattice. (c) Hexagonal unit cell of the periodic structure shown in (b). With the periodic boundary condition on its edges, this unit cell forms a hexagonal computational window. 1/12 of the computational window is shown with dashed lines. (d) A rhombus-shaped unit-cell as a computational window. 1/4 of the computational window is shown with dashed lines. Periodic boundary conditions are depicted with dotted lines.

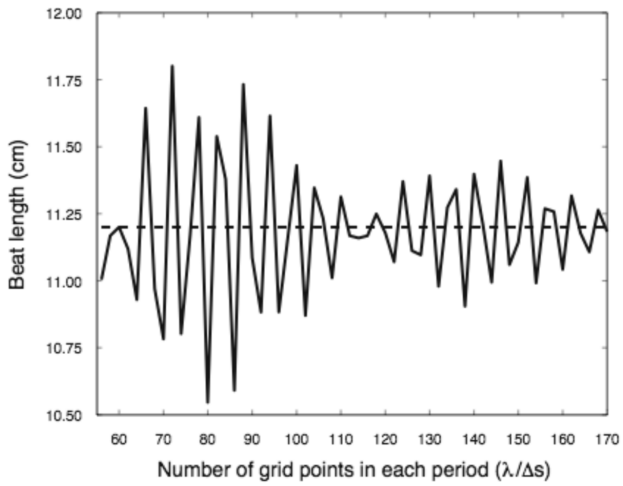

Fig. 3. Convergence of the predicted beat length for an elliptical step-index fiber with silica core and air cladding at $\lambda = 1.5\,\mu$m. The beat length calculated exactly by other means is shown as the dashed line.

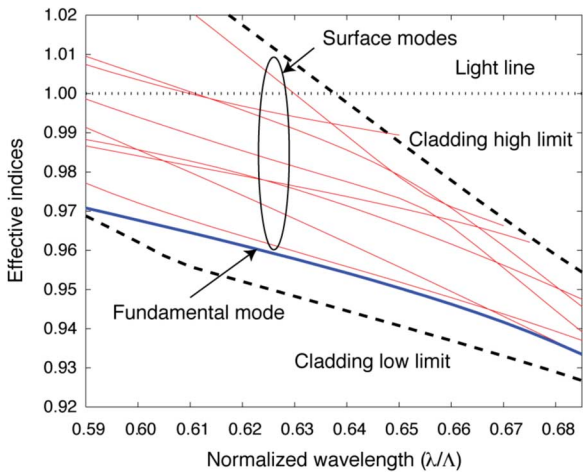

Fig. 4. Dispersion curves for all modes of the fiber shown in Fig. 2.

Strong perturbation should be used instead. In the strong perturbation model, Maxwell's equations for an unperturbed structure are reformulated into the generalized Hermitian eigenvalue problem:

$$\hat{A}|\psi_\beta\rangle = \beta\hat{B}|\psi_\beta\rangle \tag{17}$$

in which the following Dirac notation is used for transverse fields:

$$|\psi_\beta\rangle = \begin{bmatrix} \mathbf{E}_t \\ \mathbf{H}_t \end{bmatrix}. \tag{18}$$

A perturbation of the permittivity profile of a fiber, in general, changes the operator $\hat{A}$ into $\hat{A} + \Delta\hat{A}$, but leaves the operator $\hat{B}$ unchanged. The perturbed propagation constant $\tilde{\beta}$ can be obtained from the unperturbed fields and the unperturbed propagation constant β using [24]:

$$\tilde{\beta} = \beta + \frac{\langle\psi_\beta|\Delta\hat{A}|\psi_\beta\rangle}{\langle\psi_\beta|\hat{B}|\psi_\beta\rangle}. \tag{19}$$

In [24], the use of a strong perturbation method is proposed to model waveguides with an isotropic permittivity profile. Since we utilize sub-pixel averaging in our method, we need to extend

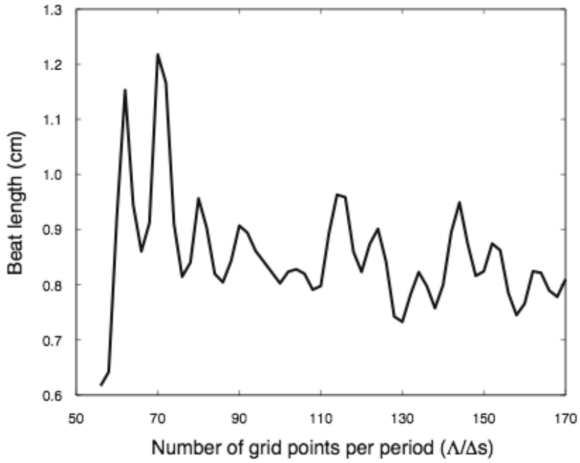

Fig. 5. The convergence of the beat length for the fiber shown in Fig. 2 with 1% ellipticity at $\lambda = 0.62\Lambda$ (far from surface modes).

this formulation to a medium with an anisotropic permittivity tensor expressed in the form:

$$\bar{\bar{\varepsilon}} = \begin{bmatrix} \varepsilon_{xx} & \varepsilon_{xy} & 0 \\ \varepsilon_{yx} & \varepsilon_{yy} & 0 \\ 0 & 0 & \varepsilon_z \end{bmatrix}. \tag{20}$$

It should be noted that this tensor is expressed in Cartesian coordinates. Hence, its elements are generally different from the elements $\varepsilon_{r1||}$ and $\varepsilon_{r1\perp}$ discussed in Section III, although it can be shown simply that they are related to them. They are calculated using the method discussed in [23]. The operators $\hat{A}$ and $\hat{B}$ can then simply be obtained by substituting this permittivity tensor for ε in (9) of [24], i.e.,

$$\hat{B} = \begin{bmatrix} 0 & -\hat{z}\times \\ \hat{z}\times & 0 \end{bmatrix} \tag{21}$$

$$\hat{A} = \begin{bmatrix} \omega\bar{\bar{\varepsilon}} - \frac{1}{\omega\mu_\circ}\nabla_t\times[\hat{z}(\hat{z}\cdot\nabla_t\times)] & 0 \\ 0 & \omega\mu_\circ - \frac{1}{\omega}\nabla_t\times\left[\hat{z}\left(\bar{\bar{\varepsilon}}^{-1}\hat{z}\cdot\nabla_t\times\right)\right] \end{bmatrix} \tag{22}$$

The scaling of the unperturbed fiber geometry in the transverse plane, in general, can be expressed in the scaled coordinates as

$$\begin{aligned} x_{\text{scaled}} &= x(1+\delta_x) \\ y_{\text{scaled}} &= y(1+\delta_y). \end{aligned} \tag{23}$$

The transverse curl of the field $\mathbf{F}$ in the scaled coordinate and in the unperturbed coordinate are related by [24]

$$\nabla_{t,\text{scaled}} \times \mathbf{F} = \nabla_t \times \mathbf{F} - \hat{O} \tag{24}$$

where

$$\hat{O} = \begin{vmatrix} \hat{x} & \hat{y} & \hat{z} \\ \eta_x\frac{\partial}{\partial x} & \eta_y\frac{\partial}{\partial y} & 0 \\ F_x & F_y & F_z \end{vmatrix} \tag{25}$$

and $\eta_x = \delta_x/(1+\delta_x)$ and $\eta_y = \delta_y/(1+\delta_y)$ [24]. Substituting (24) and (25) in (22), one obtains the operator $\hat{A}$ in the scaled coordinates

$$\hat{A}_{\text{scaled}} = \hat{A}_o + \Delta\hat{A} \tag{26}$$

where $\hat{A}_o$ is the operator $\hat{A}$ of the unperturbed fiber, which has the same form as (22), and $\Delta\hat{A}$ is shown in (27) at the bottom of the page.

Using these explicit forms of $\hat{A}$ and $\hat{B}$, we can calculate $\langle\psi_\beta|\Delta\hat{A}|\psi_\beta\rangle$ and $\langle\psi_\beta|\hat{B}|\psi_\beta\rangle$, then use (19) to find the perturbed value of the propagation constant. Since the operator $\hat{B}$ does not depend on the permittivity tensor, $\langle\psi_\beta|\hat{B}|\psi_\beta\rangle$ is identical to (19) in [24]. Therefore,

$$\langle\psi_\beta|\hat{B}|\psi_\beta\rangle = \int dS\hat{z}\cdot(\mathbf{E}_t^*\times\mathbf{H}_t + \mathbf{E}_t\times\mathbf{H}_t^*) \tag{28}$$

where the integration is carried out over the right-angle triangular computational window shown in Fig. 2(d). Using the vector identity $\mathbf{a}\cdot(\nabla\times\mathbf{b}) = \nabla\cdot(\mathbf{b}\times\mathbf{a}) + \mathbf{b}\cdot(\nabla\times\mathbf{a})$ and Maxwell's equations with the permittivity tensor of (20), and after some simplification, one arrives at (29), shown at the bottom of the page.

Consequently, to study the birefringence in PBFs with an elliptically stretched index profile, we follow the following general procedure. We first find the modes of the unperturbed PBF using the finite-difference method presented in Section III. The

$$\Delta\hat{A} = \frac{1}{\omega}\begin{bmatrix} \frac{1}{\mu_o}\nabla_t\times(\hat{z}(\hat{z}\cdot\hat{O})) + \frac{1}{\mu_o}\hat{O}(\hat{z}(\hat{z}\cdot\nabla_t\times)) & 0 \\ 0 & \nabla_t\times(\hat{z}(\bar{\bar{\varepsilon}}^{-1}\hat{z}\cdot\hat{O})) + \hat{O}\left(\hat{z}(\bar{\bar{\varepsilon}}^{-1}\hat{z}\cdot\nabla_t\times)\right) \end{bmatrix} \tag{27}$$

$$\langle\psi_\beta|\Delta\hat{A}|\psi_\beta\rangle = \int dS \begin{bmatrix} E_x \\ E_y \\ H_x \\ H_y \end{bmatrix}^\dagger \begin{bmatrix} 2\omega\varepsilon_{xx}\eta_y & \omega(\varepsilon_{yx}\eta_x + \varepsilon_{xy}\eta_y) & 0 & -\beta(\eta_x+\eta_y) \\ \omega(\varepsilon_{yx}\eta_x + \varepsilon_{xy}\eta_y) & 2\omega\varepsilon_{yy}\eta_x & \beta(\eta_x+\eta_y) & 0 \\ 0 & \beta(\eta_x+\eta_y) & 2\omega\mu_o\eta_y & 0 \\ -\beta(\eta_x+\eta_y) & 0 & 0 & 2\omega\mu_o\eta_x \end{bmatrix} \begin{bmatrix} E_x \\ E_y \\ H_x \\ H_y \end{bmatrix} \tag{29}$$

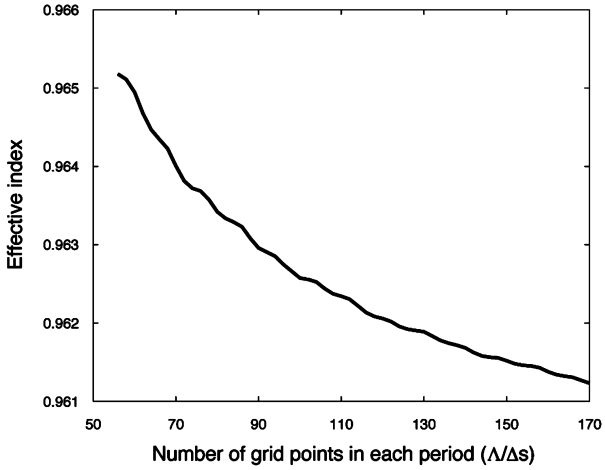

Fig. 6. Convergence of the effective index of the fundamental mode of the fiber of Fig. 2 at $\lambda = 0.62\Lambda$.

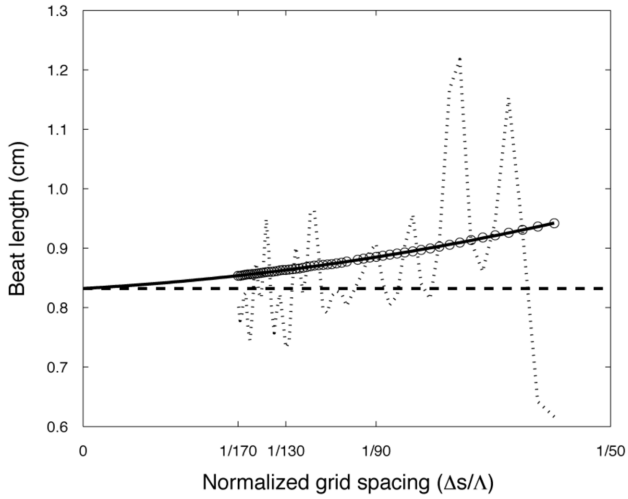

Fig. 7. Convergence of the beat length for the fiber shown in Fig. 2 with 1% ellipticity at $\lambda = 0.62\Lambda$ (circles). The solid curve shows the polynomial fit. The dashed curve shows the value of the polynomial fit at $\Delta s = 0$. The dotted curve depicts the beat length predicted by the FDFD scheme alone (reproduced from Fig. 4).

discretized values of E_x, E_y, H_x, and H_y are then obtained by using E_1, E_2, E_3, H_1, H_2, and H_3 at the points where E_1 and H_1 are defined. According to Fig. 1, $E_x = E_1$ and $H_y = H_1$. E_y and H_x are calculated approximately from the neighboring discretized fields according to

$$H_x(i,j) = -\frac{1}{2\sqrt{3}}(H_2(i,j) + H_2(i,j+1) + H_3(i,j) + H_3(i+1,j)) \quad (30)$$

$$E_y(i,j) = \frac{1}{2\sqrt{3}}(E_2(i,j) + E_2(i,j+1) + E_3(i,j) + E_3(i+1,j)). \quad (31)$$

These discretized fields are then inserted in (19), (28), and (29). Finally, the integrations in (28) and (29) are performed numerically over the right-angle triangular computational domain to find the effective indexes of the perturbed fiber modes. This process was also implemented in C++ and run on the same machines to model the same PBF as discussed in Section V.

VII. Numerical Results

We started with modeling the fiber structure with C_{6v} symmetry at several wavelengths within the bandgap. The calculated dependence of the effective index of the fundamental mode on spatial resolution at $\lambda = 0.62\Lambda$ (far from surface modes) is plotted in Fig. 6. The convergence behavior is very good: at the spatial resolution of $\Lambda/170$, the relative error is less than 1%. This fast convergence shows that sub-pixel averaging has restored the quadratic convergence rate for the effective index of the doubly degenerate mode of the fiber shown in Fig. 2. The convergence behavior at wavelengths close to surface modes is comparable. However, it should be noted that this convergence is slower than for simpler fiber structures such as step-index fibers or solid-core PCFs. This is due to the high air-filling ratio and fine structure of PBFs. The existence of surface modes also often degrades the convergence rate.

The convergence behavior of the beat length of this fiber with 1% ellipticity at $\lambda = 0.62\Lambda$ is plotted in Fig. 7 (note that the horizontal axis is the grid spacing instead of the number of grid points). For comparison, we have also shown the beat length predicted by the FDFD method alone (dotted curve). The beat length predicted by the strong-perturbation model converges very smoothly. As expected, the convergence rate of the beat length is slower than that of the effective index: the residual error at spatial resolution of $\Lambda/170$ is $\varepsilon = 0.9\%$ for the effective index (see Fig. 6), where it is 2.5% for the beat length (see Fig. 7).

In general, the error in the predicted beat length has at least three origins: the error in the finite-difference equations, the error in the strong-perturbation model, and the error in the numerical evaluation of the integrals in the strong perturbation. The error in the solution of the finite-difference equations is generally composed of a term in Δs and a term in Δs^2[28]. In addition, the error produced by the numerical evaluation of the integrals in the strong perturbation method is proportional to Δs. As a consequence, we expect that the total error in the beat length, to the lowest order, is a combination of Δs and Δs^2.

A good estimate of the error in the predicted beat length (Fig. 7) can be obtained by fitting a second-order polynomial in Δs to this curve. The value of this polynomial when $\Delta s \to 0$ then provides the expected value of the beat length [28]. This polynomial fit is shown as the solid curve in Fig. 7. Its limit at $\Delta s = 0$ yields an expected value of 0.832 cm for the beat length (dashed line in Fig. 7). Consequently, the relative error in the value predicted by the FDFD method at $\Delta s = \Lambda/170$ is around 2.5%. This polynomial fit also predicts that a spatial resolution of $\Delta s = \Lambda/364$ would be required to reduce this error to 1%. At wavelength close to a surface mode, the convergence rate of the beat length is slightly slower, but the relative error in the predicted beat length at $\Delta s = \Lambda/170$ is still less than 3%.

Fig. 7 clearly shows that the average of the beat lengths predicted by the direct use of our FDFD scheme at high spatial resolutions yields a value very close to the expected value of 0.832 cm. Consequently, there is a very good agreement between the direct approach and the strong-perturbation approach.

Our study shows that the magnitude of the oscillations in the beat length predicted by the direct approach at low spatial resolutions decreases for ellipticities higher than 1%. This is expected since the discretized structures with higher ellipticies vary less abruptly when the spatial resolution is changed. Also, the error in the beat lengths predicted by strong perturbation increases when the ellipticity, and hence the perturbation, is increased. We observed that for the PBF discussed in this paper, the values predicted by these two methods agree very well for ellipticities less than 2%. For ellipticities more than 2%, the values predicted by these methods start to deviate from each other.

VIII. Conclusion

We have developed and validated the formalism for a new full-vector finite-difference scheme, based on a hexagonal Yee's grid along with sub-pixel averaging, to solve for the modes of unperturbed photonic-bandgap fibers with perfect C_{6v} symmetry. The key advantage of this scheme is the complete absence of numerical birefringence. Moreover, this method is very easy to implement and to parallelize. Sub-pixel averaging enables fast convergence of the modes' effective indices. The computational cost can be significantly reduced by exploiting the mirror symmetry of the system. This method can also be used to analyze fibers with C_{2v} symmetry. We applied it to study the birefringence of the fundamental mode of a PBF with original C_{6v} symmetry in which an ellipticity is introduced by stretching the fiber unidirectionally along one of its transverse axes. The abrupt variations of the discretized structures with different spatial resolutions lead to an oscillatory beat length convergence behavior. However, these oscillations have small amplitudes, and averaging yields a very accurate value of the beat length. We also proposed a strong perturbation for studying the birefringence in PBFs, which performs this averaging in a systematic way. The modes of the unperturbed fiber calculated by the finite-difference method are used as inputs to the strong perturbation. As expected, this method yielded fast convergence in the effective index of the fundamental mode, at all wavelengths. It also produced a very smooth beat length convergence for all values of the fiber ellipticity. By fitting a second-order polynomial to the obtained results as a function of grid spacing, we found again accurate estimates of the beat length for ellipticities up to 2%. The strong perturbation method is therefore quite effective at reducing the intrinsic residual error of the FDFD method. We believe that these two methods will be useful for the accurate prediction of the birefringence in a large class of PBFs with deformed cross sections.

References

[1] J. C. Knight, T. A. Birks, P. S. J. Russell, and D. M. Atkin, "All-silica single mode optical fiber with photonic crystal cladding," *Opt. Lett.*, vol. 21, pp. 1547–1549, 1996.

[2] P. R. McIsaac, "Symmetry-induced modal characteristics of uniform waveguides. I. Summary of results," *IEEE Trans. Microw. Theory Tech.*, vol. 23, pp. 421–429, 1975.

[3] M. J. Steel, T. P. White, C. M. de Sterke, R. C. McPhedran, and L. C. Botten, "Symmetry and degeneracy in microstructured optical fibers," *Opt. Lett.*, vol. 26, pp. 488–490, 2001.

[4] A. Peyrilloux, T. Chartier, A. Hideur, L. Berthelot, G. Melin, S. Lempereur, D. Pagnoux, and P. Roy, "Theoretical and experimental study of the birefringence of a photonic crystal fiber," *J. Lightw. Technol.*, vol. 21, no. 2, pp. 536–539, 2003.

[5] M. J. F. Digonnet, H. K. Kim, G. S. Kino, and S. Fan, "Understanding air-core photonic bandgap fibers: Analogy to conventional fibers," *J. Lightw. Technol.*, vol. 23, pp. 4169–4177, 2005.

[6] W. Zhi, R. Guobin, L. Shuqin, and J. Shuisheng, "Supercell lattice method for photonic crystal fibers," *Opt. Express*, vol. 11, no. 9, pp. 980–991, 2003.

[7] J. G. Pearce, T. D. Hedley, and D. M. Bird, "Adaptive curvilinear coordinates in a plane-wave solution of Maxwell's equations in photonic crystals," *Phys. Rev. B*, vol. 71, no. 19, pp. 195108–1, 2005.

[8] F. Brechet, J. Marcou, D. Pagnoux, and P. Ray, "Complete analysis of the characteristics of propagation into photonic crystal fibers, by finite element method," *Opt. Fiber Technol.*, vol. 6, pp. 181–191, 2000.

[9] A. Cucinotta, S. Selleri, L. Vincetti, and M. Zoboli, "Holey fiber analysis through the finite-element method," *IEEE Photon. Technol. Lett.*, vol. 14, no. 11, pp. 1530–1532, 2002.

[10] M. Koshiba and K. Saitoh, "Numerical verification of degeneracy in hexagonal photonic crystal fibers," *IEEE Photon. Technol. Lett.*, vol. 13, no. 12, pp. 1313–1315, 2001.

[11] K. Saitoh and M. Koshiba, "Full-vectorial imaginary-distance beam propagation method based on a finite element scheme: Application to photonic crystal fibers," *J. Quantum Electron.*, vol. 38, no. 7, pp. 927–933, 2002.

[12] M. Qiu, "Analysis of guided modes in photonic crystal fibers using finite-difference time-domain method," *Microw. Opt. Technol. Lett.*, vol. 30, pp. 327–330, 2001.

[13] T. P. White, R. McPhedran, L. Botten, G. Smith, and C. M. de Sterke, "Calculations of air-guided modes in photonic crystal fibers using the multipole method," *Opt. Express*, vol. 9, no. 13, pp. 721–732, 2001.

[14] T. P. White, B. T. Kuhlmey, R. C. McPhedran, D. Maystre, G. Renversez, C. M. de Sterke, and L. C. Botten, "Multipole method for microstructured optical fibers. I. formulation," *J. Opt. Soc. Am. B*, vol. 19, no. 10, pp. 2322–2330, 2002.

[15] S. Campbell, R. C. McPhedran, C. M. de Sterke, and L. C. Botten, "Differential multipole method for microstructured optical fibers," *J. Opt. Soc. Am. B*, vol. 21, no. 11, pp. 1919–1928, 2004.

[16] Z. Zhu and T. G. Brown, "Full-vectorial finite-difference analysis of microstructured optical fibers," *Opt. Express*, vol. 10, pp. 853–864, 2002.

[17] C. Yu and H. Chang, "Applications of the finite-difference mode solution method to photonic crystal structures," *Opt. Quantum Electron.*, vol. 36, pp. 145–163, 2004.

[18] V. Dangui, M. J. F. Digonnet, and G. S. Kino, "A fast and accurate numerical tool to model the modal properties of photonic-bandgap fibers," *Opt. Express*, vol. 14, pp. 2979–2993, 2006.

[19] A. B. Sotskii and L. I. Sotskaya, "Calculation of optical properties of hollow-core photonic crystal fibers," *J. Appl. Spectroscopy*, vol. 76, no. 2, pp. 292–301, 2009.

[20] J. M. Fini, "Improved symmetry analysis of many-moded microstructure optical fibers," *J. Opt. Soc. Am. B*, vol. 21, pp. 1431–1436, 2004.

[21] A. Cucinotta, S. Sellari, L. Vincetti, and M. Zoboli, "Perturbation analysis of dispersion in photonic crystal fibers through the finite element method," *J. Lightw. Technol.*, vol. 20, pp. 1433–1442, 2002.

[22] F. Poletti, N. G. R. Broderick, D. Richardson, and T. Monro, "The effect of core asymmetries on the polarization properties of hollow-core photonic bandgap fibers," *Opt. Express*, vol. 13, no. 22, pp. 9115–9124, 2005.

[23] A. Farjadpour, D. Roundy, A. Rodriguez, M. Ibanescu, P. Bermel, J. D. Joannopoulos, S. G. Johnson, and G. W. Burr, "Improving accuracy by subpixel smoothing in the finite-difference time domain," *Opt. Lett.*, vol. 31, pp. 2972–2974, 2006.

[24] M. Skorobogatiy, M. Ibanescu, S. G. Johnson, O. Weisberg, T. D. Engeness, M. Soljacic, S. A. Jacobs, and Y. Fink, "Analysis of general geometric scaling perturbations in a transmitting waveguide: Fundamental connection between polarization-mode dispersion and group-velocity dispersion," *J. Opt. Soc. Am. B*, vol. 19, no. 12, pp. 2867–2875, 2002.

[25] S. G. Johnson and J. D. Joannopoulos, "Block-iterative frequency-domain methods for Maxwell's equations in a planewave basis," *Opt. Express*, vol. 8, no. 3, pp. 173–190, 2001.

[26] C. Yeh, "Elliptical dielectric waveguides," *J. Appl. Phys.*, vol. 33, no. 11, pp. 3235–3243, 1962.
[27] S. R. Rengarajan and J. E. Lewis, "First higher-mode cutoff in two-layer elliptical fibre waveguides," *Electron. Lett.*, vol. 16, no. 7, pp. 263–264, Mar. 1980.
[28] S. Fan, P. R. Villeneuve, and J. D. Joannopoulos, "Large omnidirectional band gaps in metallodielectric photonic crystals," *Phys. Rev. B*, vol. 54, no. 16, pp. 11245–11251, Oct. 1996.

Kiarash Zamani Aghaie (S'05) received the B.S. and M.S. degrees in electrical engineering from the University of Tehran, Tehran, Iran, in 2002 and 2005, respectively. He is currently pursuing the Ph.D. degree at Stanford University, Stanford, CA.

His research interests include numerical modeling of photonic-bandgap fibers and photonic crystals, and photonic-bandgap fiber components.

Shanhui Fan (M'05–SM'06) was an undergraduate student in physics at the University of Science and Technology of China, Hefei, Anhui, China, from 1988 to 1992, and he received the Ph.D. degree in physics from the Massachusetts Institute of Technology (MIT), Cambridge, in 1997.

He was a Postdoctoral Research Associate in Physics at MIT from 1997 to 1999 and a Research Scientist at the Research Laboratory of Electronics, MIT, from 1999 to 2001. He is an Associate Professor of electrical engineering at Stanford University, Stanford, CA. He has been at Stanford University since 2001. His interests include theory and simulations of photonic and solid-state materials and devices, photonic crystals, nanoscale photonic devices and plasmonics, quantum optics, computational electromagnetics, and parallel scientific computing. He has published over 140 journal articles, has given more than 100 invited talks, and holds 28 granted U.S. patents.

Dr. Fan received the Adolph Lomb Medal from the Optical Society of America, the National Academy of Sciences Award for Initiative in Research, a David and Lucile Packard Fellowship, and a National Science Foundation Career Award. He is a Fellow of OSA, APS, and SPIE.

Michel J. F. Digonnet received the degree of engineering from Ecole Supérieure de Physique et de Chimie de la Ville de Paris, the Diplome d'Etudes Approfondies in coherent optics from the University of Paris, Orsay, France, in 1978, and the M.S. and Ph.D. degrees from the Applied Physics Department of Stanford University, Stanford, CA, in 1980 and 1983, respectively. His doctoral research centered on WDM fiber couplers and fiber lasers and amplifiers.

He is a Professor of applied physics at Stanford University. From 1983 to 1986, he was employed by Litton Guidance and Control, Chatsworth, CA, as a Visiting Scholar at Stanford, conducting research in miniature solid-state sources and integrated optics for fiber sensors. From 1986 to 1990, he was involved in the development of dye and 2-μm solid-state lasers, fiber sensors and delivery systems for laser angioplasty at MCM Laboratories, Mountain View, CA. His current interests include photonic-bandgap fibers, fiber sensor arrays, slow light in sensors, and fiber-based MEMS sensors. He has published 240 articles, holds 78 U.S. patents, edited several books, and chaired numerous conferences on optical fiber devices and fiber sensors. He teaches courses on fiber amplifiers, lasers, and fiber sensors.